

Effect on the Electronic and Magnetic Properties of Antiferromagnetic Topological Insulator MnBi_2Te_4 with Sn Doping

Susmita Changdar,¹ Susanta Ghosh,¹ Kritika Vijay,^{2,3} Indrani Kar,¹ Sayan Routh,¹
P. K. Maheswari,¹ Soumya Ghorai,¹ Soma Banik,^{2,3} and S. Thirupathaiah^{1,*}

¹*Condensed Matter Physics and Material Sciences Department,*

S. N. Bose National Centre for Basic Sciences, Kolkata, West Bengal-700106, India.

²*Synchrotrons Utilization Section, Raja Ramanna Centre for Advanced Technology, Indore 452013, India.*

³*Homi Bhabha National Institute, Training School Complex, Anushakti Nagar, Mumbai, 400094, India.*

(Dated: July 28, 2022)

We thoroughly investigate the effect of nonmagnetic Sn doping on the electronic and magnetic properties of antiferromagnetic topological insulator MnBi_2Te_4 . We observe that Sn doping reduces the out-of-plane antiferromagnetic (AFM) interactions in MnBi_2Te_4 up to 68% of Sn concentration, and above the system is found to be a paramagnetic. In this way, the anomalous Hall effect observed at a very high field of 7.8 T in MnBi_2Te_4 is reduced to 2 T with 68% of Sn doping. Electrical transport measurements suggest that all compositions are metallic in nature, while the low temperature resistivity is sensitive to the AFM ordering and to the doping induced disorder. Hall effect study demonstrates that Sn actually dopes electrons into the system, thus, enhancing the electron carrier density almost by two orders at 68% of Sn. In contrast, SnBi_2Te_4 is found to be a p-type system. Angle-resolved photoemission spectroscopy (ARPES) studies show that the topological properties are intact at least up to 55% of Sn as the Dirac surface states are present in the valance band, but in SnBi_2Te_4 we are unable to detect the topological states due to heavy hole doping. Overall, Sn doping significantly affects the electronic and magnetic properties of MnBi_2Te_4 .

I. INTRODUCTION

Introduction of magnetism into a topological insulator has been known to give rise to various exotic quantum phenomena such as Axion [1–3] and Chern insulating states, [4–6], Majorana zero modes [7], and Weyl semimetallic phase [8–10]. However experimental realization of such peculiar systems has been quite challenging due to the lack of intrinsic magnetism in topological insulators. Earlier, magnetic ordering in the topological insulators, $(\text{Bi}/\text{Sb})_2\text{Te}_3$, was achieved by doping with the magnetic ions like Cr/V [4, 5, 11, 12] in order to induce quantum anomalous Hall insulating (QAH) phase. In this way, a ferromagnetic (FM) order is induced to break the time reversal symmetry (TRS) in the system. When TRS breaks, the degeneracy of surface Dirac point is lifted and the gap opening is followed by the chiral edge states, responsible for the QAH effect as observed in these systems. However, so far this method showed QAH states at very low temperatures (< 1 K) [5, 13].

Interestingly, MnBi_2Te_4 was recently discovered to be one of such intrinsic topological insulator with spontaneous AFM order [14–25], in which the layers of ferromagnetically ordered Mn ions are coupled antiferromagnetically along the c -axis. Here, the long range magnetic ordering breaks TRS but the combination of TRS (Θ) and half-lattice translational operator ($T_{1/2}$) connecting the two nearest Mn layers, i.e. $S = \Theta T_{1/2}$ remains protected [19]. As a result, MnBi_2Te_4 becomes a potential candidate for hosting intriguing topological properties. It was also found that MnBi_2Te_4 thin flakes exhibit Axion insulating state for even number of layers [26]. Chern insulating state is noticed

for odd number of layers at zero magnetic field [17]. But at much higher magnetic fields even number of layers also show Chern insulating phase [26]. Similar to even number layered thin flakes, bulk MnBi_2Te_4 shows magnetization, thus requiring a very high magnetic fields (7.8 T) to obtain the QAH effect [27]. One approach to see QAH effect in MnBi_2Te_4 at lower fields is by weakening the interlayer AFM exchange coupling by doping with nonmagnetic ion like Sn at the Mn site.

In this work, we report comprehensively on the effect of Sn doping on the electronic and magnetic properties of the magnetic topological insulator MnBi_2Te_4 . For this, we studied various single crystals of $\text{Mn}_{1-x}\text{Sn}_x\text{Bi}_2\text{Te}_4$ with $x=0, 0.2, 0.55, 0.68, 0.86, \text{ and } 1$. We realized that Sn doping has a significant effect on the antiferromagnetic (AFM) ordering. That is, we observe a decrease in Néel temperature (T_N) from 24 K for MnBi_2Te_4 to 6 K for 68% of Sn doping, while $x=0.86$ and 1 are found to be paramagnetic in nature. Further, we observe that the out-of-plane magnetic ordering is intact up to $x=0.68$, while for in-plane there is a change from linear $M(H)$ behaviour to a very weak ferromagnetic type $M(H)$ curve with a saturated magnetization of $0.8 \mu_B/\text{f.u}$ with increasing Sn. We find a cusp on the resistivity data at the Néel temperature, which decreases with increasing Sn up to $x=0.2$, consistent with magnetic studies. However, as the Sn doping increased beyond $x=0.2$, we do not observe cusp at respective Néel temperatures but rather we observe low temperature resistivity upturn due to Sn doping induced disorder. On the other hand, SnBi_2Te_4 show Fermi-liquid type resistivity as the disordered is significantly reduced by fully replacing Mn with Sn. We further notice that Sn induces electron carriers into MnBi_2Te_4 . As a result, the electron carrier concentration increase by two orders at a Sn concentration of 68% compared to MnBi_2Te_4 . In contrast to MnBi_2Te_4 , SnBi_2Te_4 is found to be a p-type system. The Fermi level shift in the electronic band

* setti@bose.res.in

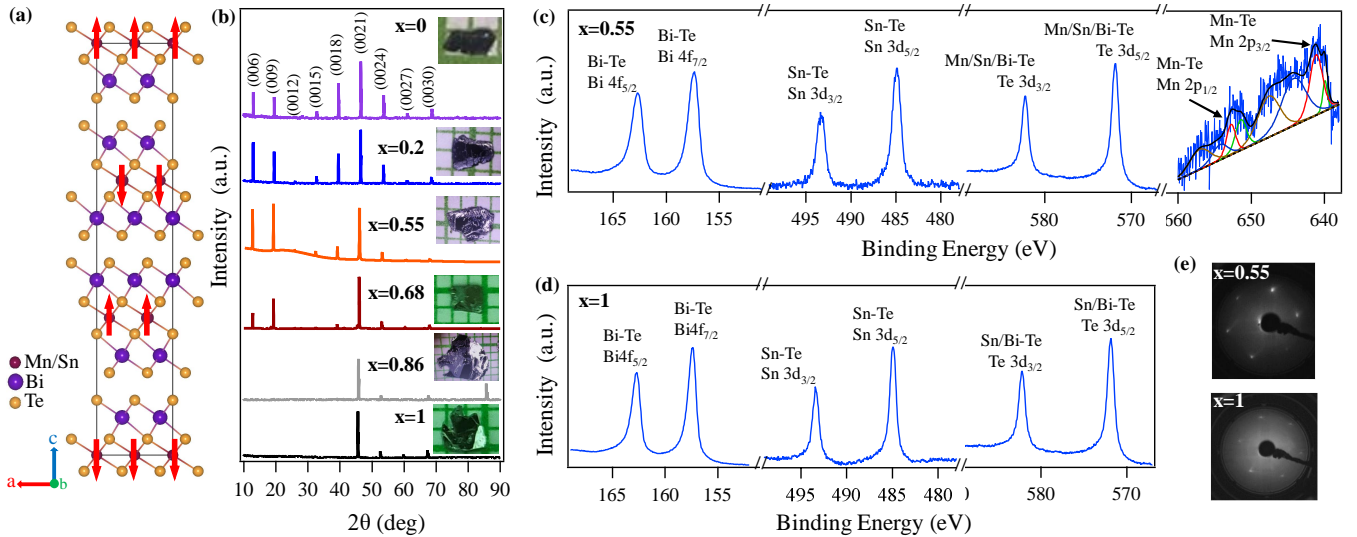


FIG. 1. (a) Rhombohedral crystal structure of MnBi₂Te₄. Red arrows indicate the Mn²⁺ ion spins in AFM state. (b) Single crystal XRD patterns showing (00l) reflections from all the compositions. Insets in (b) show single-crystal photographic images of each doping concentration on which the measurements were done. (c) and (d) Show XPS spectra exhibiting the Bi 4f, Sn 3d, Te 3d, and Mn 2p core levels for x=0.55 and Bi 4f, Te 3d, and Sn 3d core levels for x=1, respectively. (e) Shows LEED data taken with 70 eV photon energy revealing hexagonal pattern for both x=0.55 and x=1 single crystals.

dispersions observed from ARPES studies on x=0.55 and x=1 single crystals is consistent with carrier concentrations estimated from the Hall measurements. We further notice that the topological properties are intact up to 55% of Sn doping as the surface Dirac states are present in the valance band, while in SnBi₂Te₄ we are unable to detect them due to heavy hole doping.

II. EXPERIMENTAL DETAILS

We synthesized high quality single crystals of Mn_{1-x}Sn_xBi₂Te₄ with x=0, 0.2, 0.55, 0.68, 0.86, and 1 using the solid state reaction route [27]. Constituent elements of Mn (99.9%), Sn (99.99%), Bi (99.99%), and Te (99.99%) were taken in stoichiometric ratio, mixed thoroughly in argon atmosphere, and kept in an alumina crucible before sealing it in a quartz ampoule under a vacuum of 10⁻⁴ mbar. The sealed quartz ampoule was then heated in a chamber furnace up to 900°C at a rate of 150°C/hr, and kept at that temperature for 24 hours. The ampoule was then cooled at a rate of 2°C/hr. The growth temperature of MnBi₂Te₄ is 590°C and for SnBi₂Te₄ it is 600°C [28]. After the controlled cooling, we performed prolonged annealing within the temperature range of 590°C to 600°C for a maximum of seven days depending on the amount of Sn doping concentration. Finally, the ampoule was quenched in cold water. In this way, we got shiny and plate-like single crystals with a maximum size of 3×3 mm².

As grown single crystals were structurally analyzed using the high-resolution X-ray diffractometer (Rigaku smartLab 9 kW) having Cu-K_α radiation. The chemical composition of the crystals were thoroughly examined

using energy dispersive X-ray spectroscopy (EDS) on cleaved sample surfaces [see Fig. S1 in supplemental information]. For convenience, herein, we will use respective nominal composition to represent each sample. Transport and magnetic properties were measured using Quantum Design Physical Property Measurement System (PPMS) with magnetic field up to 9 Tesla by varying the temperature between 2 and 300 K during the measurements. XPS and ARPES measurements were performed at the undulator based Angle Resolved Photoelectron Spectroscopy beamline (ARPES BL-10), Indus-2, India. All samples were cleaved in-situ in the vacuum better than 5×10⁻¹¹ mbar and performed low energy electron diffraction (LEED) measurements using SPECS ErLEED 1000A to examine the sample surface quality. Both the XPS and ARPES measurements were carried out at a sample temperature of 20 K using SPECS Phoibos150 electron analyser. ARPES measurements were performed with a photon energy of $h\nu = 70$ eV. The energy and angular resolutions were set at 40 meV and 0.1°, respectively, for the ARPES studies. XPS measurements were performed with a photon energy of $h\nu = 800$ eV and at an energy resolution of 0.4 eV.

III. RESULTS AND DISCUSSION

MnBi₂Te₄ crystallizes in the rhombohedral structure with a space group of R $\bar{3}m$, consists Te-Bi-Te-Mn-Te-Bi-Te septuple layers as shown in Fig. 1(a). Fig. 1(b) shows the XRD data of Mn_{1-x}Sn_xBi₂Te₄ single crystals for x=0, 0.2, 0.55, 0.68, 0.86, and 1. XRD data of all crystals show clear reflections from (00l) plane without any impurity peaks, confirming phase purity for all the crystals. Low energy electron diffraction

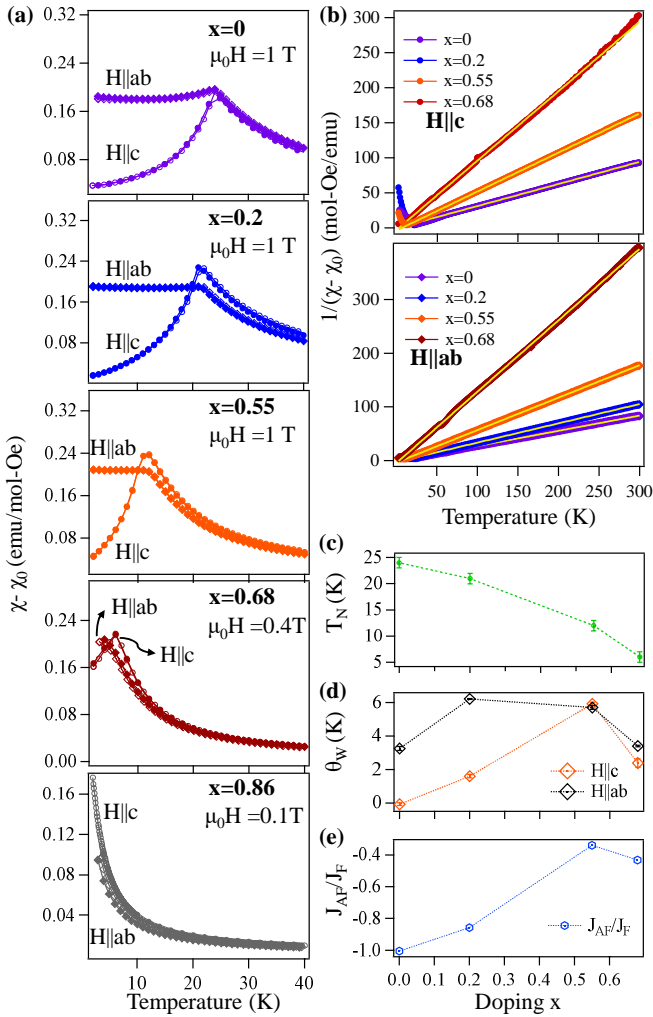


FIG. 2. (a) Temperature dependent magnetic susceptibility (χ) measured in field-cooled and zero field-cooled modes with $H \parallel c$ and $H \parallel ab$. (b) Inverse magnetic susceptibility plotted as a function of temperature with $H \parallel c$ and $H \parallel ab$. Doping dependent (c) Néel temperature (T_N), (d) Curie temperature (θ_W) for $H \parallel c$ and $H \parallel ab$, and (e) J_{AF}/J_F for $H \parallel c$.

(LEED) images taken on the freshly cleaved surfaces of $x=0.55$ and $x=1$ single crystals are shown in Fig. 1(e). The LEED pattern of both samples are in hexagonal symmetry with clear first order diffraction spots coming from (001) crystal planes. This is in good agreement with the XRD data, again confirming the high quality of single crystals. XPS data collected on $x=0.55$ and $x=1$ samples are shown in Figs. 1(c) and 1(d), respectively. Both crystals exhibit major core level peaks at 157.35 eV of Bi $4f_{5/2}$ and 162.75 eV of Bi $4f_{7/2}$, which can be assigned to the Bi³⁺ ions from the Bi-Te bond [29, 30]. Additionally, we noticed two major peaks of Sn $3d_{3/2}$ and Sn $3d_{5/2}$ at 484.85 eV and 493.3 eV, respectively, from Sn²⁺ ions associated to the Sn-Te bond [31]. Te $3d$ core levels at 582.2 eV (Te $3d_{3/2}$) and 571.85 eV (Te $3d_{5/2}$) corresponding to the Te²⁻ ions from Sn-Te, Mn-Te, and Bi-Te bonds of Mn_{0.45}Sn_{0.55}Bi₂Te₄ [32] and also from Sn-Te,

and Bi-Te bonds in SnBi₂Te₄. The peaks corresponding to Mn²⁺ from Mn-Te bonds appear at 641.1 eV of Mn $2p_{1/2}$ and 652.8 eV of Mn $2p_{3/2}$ [27, 33]. We further noticed a few low intensity peaks related to Mn²⁺ at 639.9 eV and 651.45 eV of the Mn-O bond as observed in a previous report on this system [27].

To elucidate the effect of Sn doping on the magnetic properties of MnBi₂Te₄, we performed thorough magnetic measurements on various Sn doping concentrations. Fig. 2(a) depicts field-cooled (FC) and zero-field-cooled (ZFC) magnetic susceptibility (χ) plotted as a function of temperature up to 40 K with magnetic field applied in-plane ($H \parallel ab$) and out-of-plane ($H \parallel c$) orientations. The FC and ZFC curves overlap for all samples, suggesting negligible magnetic hysteresis. In agreement with the previous reports [18, 27], MnBi₂Te₄ shows AFM ordering at a Néel temperature (T_N) of 24 K, thereby causing a sharp decrease in the magnetic susceptibility below T_N for $H \parallel c$, whereas the magnetic susceptibility for $H \parallel ab$ remains almost constant below T_N . Next with increasing Sn substitution in Mn_{1-x}Sn_xBi₂Te₄, the 2D ferromagnetic sublattice gets diluted, causing the decrease in T_N linearly from 24 K for $x=0$ to 6 K for $x=0.68$ as shown in Fig. 2(c). The large decrease in T_N implies a significant weakening of interlayer AFM coupling, while the overall AFM ordering is intact up to 68% of Sn concentration. An earlier magnetic study suggested for a magnetic transition from AFM to paramagnetic for the 66% of Sn doped Mn_{1-x}Sn_xBi₂Te₄ [34]. The discrepancy between our study and that of Ref. 34 could be that the low temperature AFM ordering is dominated by the applied magnetic field when measured with 1 T [see Fig. S2 in supplemental information]. Thus, we measured the magnetic data with a field of 0.4 T to see the AFM ordering at 6 K for $x=0.68$.

Fig. 2(b) shows the inverse magnetic susceptibility plotted as a function of temperature with $H \parallel c$ and $H \parallel ab$. From the Curie-Weiss law fitting to the data, we obtained Curie-Weiss temperature (θ_W) for each composition and is plotted in Fig. 2(d) as a function of Sn concentration. Earlier reports on MnBi₂Te₄ showed positive Curie-Weiss temperature for $H \parallel ab$ due to the in-plane FM exchange interaction and a negative Curie-Weiss temperature for $H \parallel c$ due to the out-of-plane AFM interactions [27]. In agreement to that, we obtained $\theta_W^{ab} = 3$ K and $\theta_W^c = -0.08$ K with an effective magnetic moment $\mu_{eff} = 5.3\mu_B/\text{Mn}$ for MnBi₂Te₄ [16]. The estimated μ_{eff} value matches very well with that of Mn²⁺ ions with spin $J = 5/2$ [27]. As shown in Fig. 2(d), we found different Curie-Weiss temperatures for in-plane (θ_W^{ab}) and out-of-plane (θ_W^c) field directions for the samples $x=0$ and 0.2, but at higher Sn concentrations both Curie-Weiss temperatures become almost equal due to decreasing magnetic anisotropy with increasing Sn concentration.

Moreover, both θ_W^{ab} and θ_W^c are found to be positive for $x=0.2$ and for other higher Sn concentrations, suggesting for dominating FM interactions with increasing Sn. The strength of FM exchange interaction with respect to AFM can be determined from the ratio of θ_W/T_N , which equals to $(J_F + J_{AF})/(J_F - J_{AF})$ [35]. Here J_F is intralayer

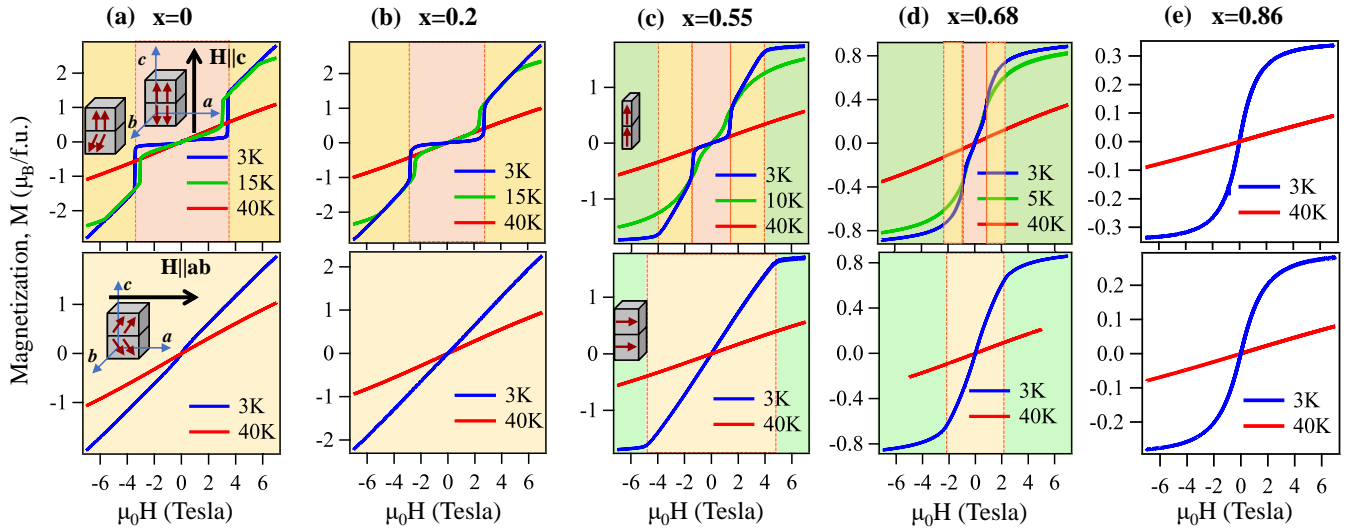


FIG. 3. Magnetization isotherms taken from (a) $x=0$, (b) $x=0.2$, (c) $x=0.55$, (d) $x=0.68$, and (e) $x=0.86$ for the field applied parallel to c -axis ($H||c$) (top figure) and parallel to ab -plane ($H||ab$) (bottom figure) measured up to 7 T. The insets are schematics representing the Mn spins in their respective color regions for two nearest Mn inter-layers (SLs).

FM exchange coupling and J_{AF} represents interlayer AFM exchange coupling. The calculated J_{AF}/J_F ratio is plotted in Fig. 2(e) as a function of doping concentration. For $MnBi_2Te_4$, J_{AF}/J_F is found to be -1 , which indicates stronger AFM exchange coupling between two Mn-layers. Increase in Sn concentration weakens the AFM coupling, thereby, decreases the J_{AF}/J_F ratio as shown in Fig. 2(e). Although the J_{AF}/J_F ratio is relatively low for doped systems ($J_{AF}/J_F = -0.43$ for $x=0.68$) compared to the parent $MnBi_2Te_4$ ($J_{AF}/J_F = -1$), it is much higher than $MnBi_4Te_7$ [$J_{AF}/J_F \approx -0.04$] [36].

Figs. 3(a)-(e) show field dependent magnetization $M(H)$ isotherms measured with $H||c$ and $H||ab$. The crystallographic c -axis is known to be spin-easy axis for $MnBi_2Te_4$. In agreement to this, Fig. 3(a) shows a spin-flop (SF) transition at a critical field of $H_c^{SF} = 3.3$ T for $H||c$ at 3 K, which gradually decreases to lower fields with increasing temperature up to the Néel temperature. Beyond the Néel temperature, the system transforms to paramagnetic (PM) in nature. During the spin-flop transition, the spin-structure of the system switches from an AFM state to a canted-AFM (CAFM) state, which upon further increase in magnetic field reaches to FM state due to complete polarization of the spins at a critical field of $H_c^{FM} = 7.8$ T for $MnBi_2Te_4$ [27]. With increasing Sn concentration, the spin-flop transition critical field decreases for $H||c$. That means, for $x=0.2$ the critical field of spin-flop transition $H_c^{SF} = 2.5$ T [see Fig. 3(b)], which gradually goes down to $H_c^{SF} = 0.7$ T for $x=0.68$ [see Fig. 3(d)]. These observations further support our earlier argument that the AFM transition in $x=0.68$ sample can be detected only with the magnetic fields below 0.7 T. Further increase in Sn concentration to $x=0.86$, the spin-flop transition is completely disappeared and the system turns to be a very weak ferromagnet as it shows a sigmoid-like $M(H)$ isotherm at 3 K for $H||c$ [see Fig. 3(e)].

Increase in Sn concentration not only decreases the spin-flop critical fields [H_c^{SF}], but also the saturation magnetization (M_S). $MnBi_2Te_4$ is known to show a saturation magnetization of $3.56 \mu_B/f.u.$ at 8 T for $H||c$ [37], it goes down to a negligible saturation magnetization of $0.32 \mu_B/f.u.$ for $x=0.86$. In fact at 3 K, we notice magnetization saturation at 4 T for $x=0.55$ and at 2.2 T for $x=0.68$ due to weak FM ordering induced with Sn doping. On the other hand, for $H||ab$, the magnetization $M(H)$ isotherms of $x=0, 0.2$, and 0.55 show linear dependents on H due to gradual polarization of spins towards the applied field direction. However, the magnetic saturation is noticed for $x=0.55$ at around 5 T. Interestingly, for $x=0.68$ and 0.86 the nature of the $M(H)$ curves at lower fields resembles to a weak ferromagnet with sigmoid-like shape and magnetic saturation is around 2 T. These observations suggest that Sn doping into $MnBi_2Te_4$ transforms the system to a weak ferromagnet.

Next, field dependent magnetoresistance (MR) up to 9 T measured at various temperatures for all compositions are plotted in Figs. 4(a)-(f). During the measurements, the magnetic field was applied along the c -axis with current applied parallel to ab -plane. From Fig. 4(a), we can see that $\rho_{xx}(H)$ of $MnBi_2Te_4$ jumps suddenly at a critical field of 3.2 T when measured below T_N , and again slope changes at a critical field of 7.8 T. The critical fields found from MR data are matching very well with that of H_c^{SF} and H_c^{FM} from the $M(H)$ data. We notice that the field dependent MR behaviour is consistent with $M(H)$ data up to Néel temperature, and above T_N we observe a parabolic field dependent MR, in agreement with an earlier report [36]. Also, the critical fields decrease monotonically with increasing Sn as demonstrated in Fig. 4(g). Next, $x=0.86$ and $x=1$ ($SnBi_2Te_4$) show parabolic field dependent MR at all the measured sample temperatures due to their paramagnetic nature [see Figs. 4(e) and 4(f)].

Temperature dependent in-plane resistivity (ρ_{xx}) data are

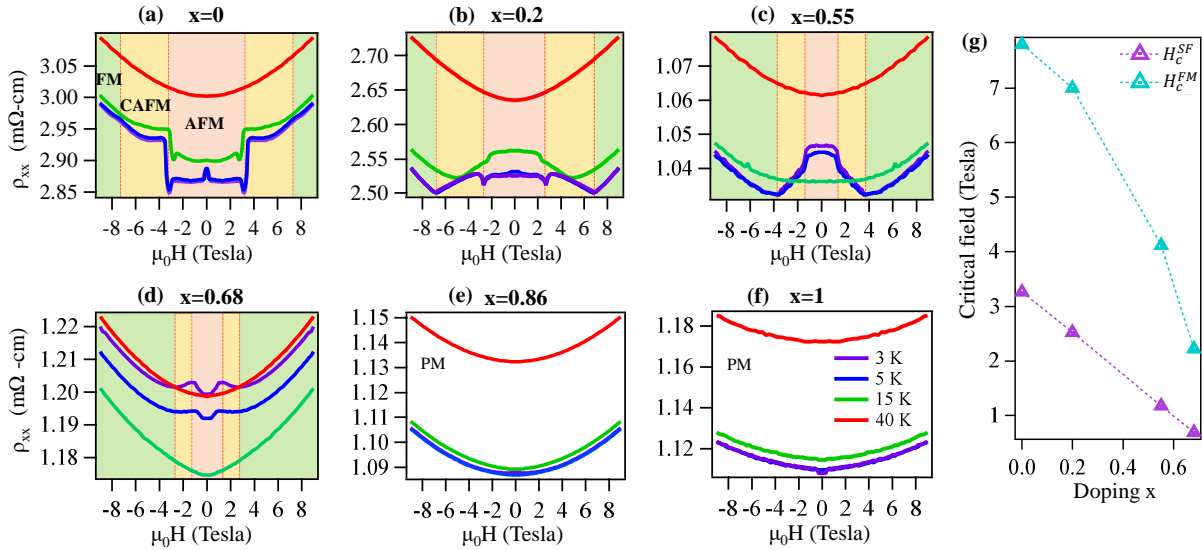


FIG. 4. Field dependent magnetoresistance (ρ_{xx}) from (a) $x=0$, (b) $x=0.2$, (c) $x=0.55$, (d) $x=0.68$, (e) $x=0.86$, and (f) $x=1$ measured at 3 K, 5 K, 15 K, and 40 K. (g) Shows doping dependent critical fields of spin-flop transition (H_c^{SF}) and ferromagnetic ordering magnetic moment saturation (H_c^{FM}).

plotted in Fig. 5(a). ρ_{xx} of all samples suggest an overall metallic behavior. We notice a cusp on the resistivity at 24 K for $x=0$ and 21 K for $x=0.2$, due to the spin-fluctuations triggered at respective Néel temperatures. On the other hand, the compositions with higher Sn such as $x=0.55$ and $x=0.68$ we find no effect of AFM ordering on ρ_{xx} data at their respective T_N 's. But both these compositions show upturn resistivity with minima at 15 K for $x=0.55$ and at 28 K for $x=0.68$. Note here that these temperature minima are higher than their respective Néel temperatures, suggesting rather a different mechanism for increasing resistivity at low temperatures such as the disorder induced electron-electron ($e-e$) interactions [38], weak localization (WL) [39], or the Kondo effect [40]. In order to explore further on the origin of resistivity upturn, we performed field dependent resistivity on $x=0.68$ and plotted the data as shown in Fig. 5(b). From Fig. 5(b) we can see that up to 9 T the resistivity upturn does not suppress, contradicting to the possibility of Kondo effect or weak localization in which case the resistivity upturn suppresses [40, 41]. Thus, low temperature resistivity upturn found could be originated from the induced disorder with Sn doping [38, 42, 43]. Nevertheless, the resistivity upturn is absent from SnBi_2Te_4 compound and rather we find a clean Fermi-liquid type resistivity curve that is satisfying the T^2 law.

Field dependent Hall resistivity (ρ_{xy}) measurements at 3 K for all compositions are shown in Fig. 5(c). As can be seen from Fig. 5(c), the $\rho_{xy}(H)$ decreases with increasing Sn concentration up to $x=0.68$ and then slope reverses the sign for SnBi_2Te_4 . The change in slope of $\rho_{xy}(H)$ clearly hints at increase in electron carrier concentration up to $x=0.68$ and then the system SnBi_2Te_4 becomes a p-type when Mn is totally replaced by Sn. To explore the Hall resistivity in details, we plotted $\rho_{xy}(H)$ individually for every composition as shown Fig. 5(d). From a closer look on the Hall data

of MnBi_2Te_4 we can notice a change in slope at the spin-flop critical field $H_c^{SF}=3.2$ T and the ferromagnetic ordering critical field $H_c^{FM}=7.8$ T. The change in slope at the critical fields is due to the anomalous Hall effect. With increasing Sn concentration, the slope change in Hall resistivity appears at much lower fields of $H_c^{SF}=0.8$ T and $H_c^{FM}=2$ T when measured on $x=0.68$ sample. These observations clearly demonstrate the tuning of anomalous Hall effect from higher fields to lower fields in going from parent to 68% of Sn doping. However, we do not observe AHE from $x=0.86$ and $x=1$ samples as they are the paramagnetic in nature.

Next, the charge carrier concentration has been estimated from the Hall data and plotted in Fig. 6 (e) for all the compositions. We calculated an electron carrier density of $5.4 \times 10^{19} \text{ cm}^{-3}$ for $x=0$, $8.18 \times 10^{19} \text{ cm}^{-3}$ for $x=0.2$, $4.59 \times 10^{20} \text{ cm}^{-3}$ for $x=0.55$, $1.2 \times 10^{21} \text{ cm}^{-3}$ for $x=0.68$, and $1.04 \times 10^{21} \text{ cm}^{-3}$ for $x=0.86$. Thus, in going from $x=0$ to $x=0.68$ the electron carrier density increased by an order of 2 and then starts decreasing. On the other hand, for $x=1$ (SnBi_2Te_4) we estimated a hole carrier density of $1.39 \times 10^{21} \text{ cm}^{-3}$, which is in good agreement with previous reports on hole carrier concentration of SnBi_2Te_4 [44–46]. Further, our observation of increase in electron density with Sn doping is in good agreement with a previous report [34].

In order to understand the effect of Sn doping on the electronic band dispersions near the Fermi level, we performed ARPES measurements on $x=0.55$ and $x=1$ single crystals as shown in Fig. 6 measured with 70 eV photon energy of linearly polarized light. Figs. 6(a) and 6(b) depict energy distribution maps (EDMs) plotted for $x=0.55$ and $x=1$, respectively, along $\bar{\Gamma}-\bar{M}$ orientation as schematically shown in the inset. Figs. 6(c) and 6(d) depict zoomed-in images of 6(a) and (b), respectively, showing band dispersions near the Fermi level. From Fig. 6(c), we can notice surface Dirac

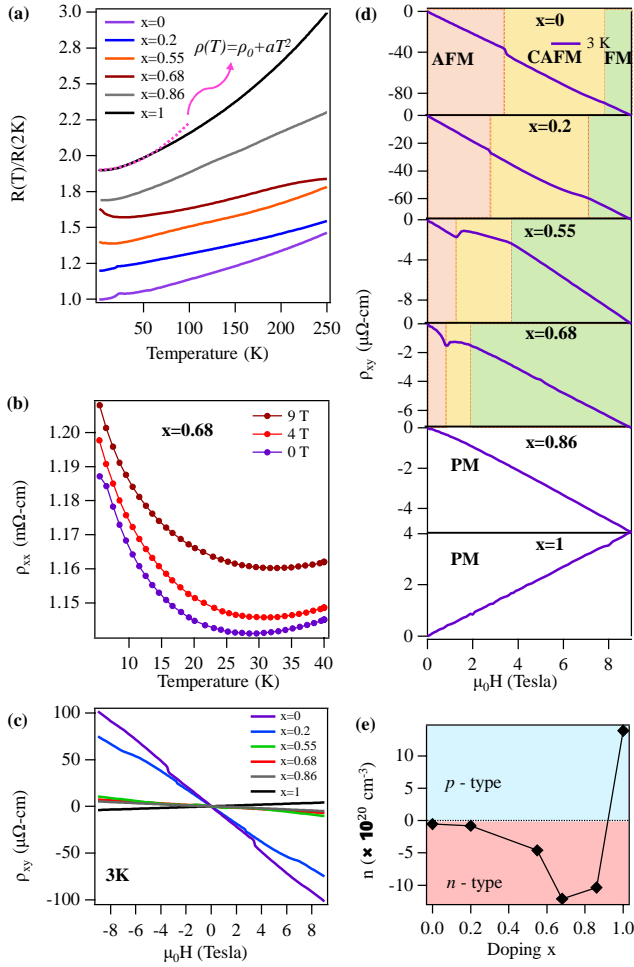


FIG. 5. (a) Stacked in-plane resistivity (ρ_{xx}) plotted as a function of temperature from all the samples. Inset shows normalized in-plane resistivity ($R(T)/R(2K)$) vs. temperature curve at low temperature. (b) ρ_{xx} vs. temperature data for $x=0.68$, measured with 0 T, 4 T, and 9 T applied magnetic field along crystallographic c -axis of the single crystal. (c) and (d) Field dependent Hall resistivity (ρ_{xy}) measured at 3 K. (red, yellow, green, and white colored regions in (d) signifies AFM, canted-AFM, FM, and PM states of the system, respectively.) (e) Charge carrier density (n) plotted as a function of Sn doping concentration.

state with a band crossing point at a binding energy of 0.23 eV as usually observed in $MnBi_2Te_4$ [22, 47, 48]. The band crossing point is estimated with the help of energy dispersive curve (EDC) extracted by integrating the EDM around $k_{\parallel}=0$, overlapped on the EDM. However, the surface Dirac state completely shifted above the Fermi level when Mn is totally replaced by Sn [see Fig. 6(d)] due to Fermi level shifting towards higher binding energy. This is in good agreement with the dominant hole carrier density estimated from the Hall measurements in the case of $SnBi_2Te_4$. Overall, the band dispersions of $MnBi_2Te_4$ along $\bar{\Gamma}-\bar{M}$ orientation are in good agreement with previous reports [49]. Though we are unable to resolve surface and bulk bands more clearly near the Fermi level within our experimental energy resolution (40 meV), the

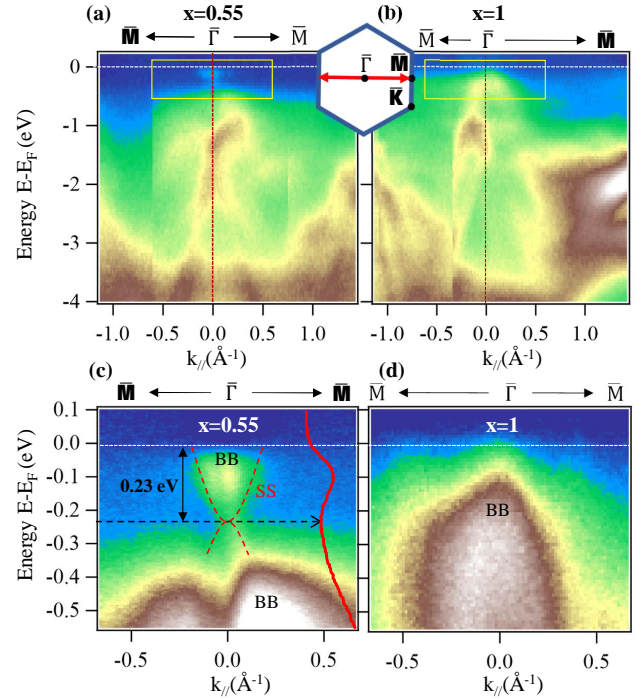


FIG. 6. (a) and (b) Energy distribution maps (EDMs) of $x=0.55$ and $x=1$, respectively, taken along $\bar{\Gamma}-\bar{M}$ direction with 70 eV photon energy using linearly polarized light. (c) and (d) are the zoomed-in EDMs of $x=0.55$ and $x=1$ near E_F . The red curve in $x=0.55$ is the energy distribution curve taken by integrating around the $\bar{\Gamma}$ point.

main message is clear that the topological Dirac surface states are intact at least up to 55% of Sn doping in $MnBi_2Te_4$. On the other hand, the bulk band dispersions look almost identical between $x=0.55$ and $x=1$, except that the bulk bands shifted towards the Fermi level in $x=1$ compared to $x=0.55$.

Despite $MnBi_2Te_4$ being topological insulator with intrinsic magnetic ordering, there are mainly two obstacles on the path of realizing Chern insulating state in this system. One of them is the high magnetic fields needed to obtain FM order [47] and the other one is the dominant bulk electron carriers induced by the excess Bi and the antisite defects in single crystals [50], shifting the Fermi level into the bulk conduction band. Doping Sn at the Mn site appeared to be a promising technique for suppressing the n-type bulk carriers as $SnBi_2Te_4$ is isostructural to $MnBi_2Te_4$ and has high p-type carrier concentration [45]. But the magnetism, an important ingredient to realize the Chern insulating state [51], seems to be disappearing beyond 68% of Sn doping while still the electron carriers dominating the transport. On the other hand, when the electron density decreased at higher Sn doping ($x=0.86$) the system turns into nonmagnetic [see Fig. 5].

IV. CONCLUSIONS

In conclusion, we have successfully grown high quality single crystals of $Mn_{1-x}Sn_xBi_2Te_4$ ($x=0, 0.2, 0.55, 0.68, 0.86$ and 1). We noticed that Sn doping in $MnBi_2Te_4$ is an effective

way of acquiring quantum Hall state at lower magnetic fields as the critical field of FM ordering goes from 7.8 T to 2 T in going from $x=0$ to $x=0.68$. Electrical resistivity is found to be sensitive to the AFM ordering temperature (T_N), but with Sn doping the low temperature resistivity shows upturn due to the doping induced disorder. However, low temperature upturn is absent in SnBi_2Te_4 as the disorder is reduced. Hall effect study shows electron doping into the system with Sn, and thus, enhancing the electron carrier density almost by two orders with 68% of Sn concentration. In contrast, SnBi_2Te_4 is found to be a p-type system. ARPES studies show that topological properties are intact up to 55% of Sn doping, but the Dirac surface states disappeared in SnBi_2Te_4 as they

moved to conduction band due to heavy hole doping. Thus, our studies clearly demonstrate the effect of Sn doping on the electronic and magnetic properties of MnBi_2Te_4 .

V. ACKNOWLEDGEMENT

S.C. acknowledges University Grants Commission (UGC), India for the Ph.D. fellowship. S.T. acknowledges financial support by the Department of Science and Technology (DST) through the grant no. SRG/2020/000393. Dr. Tapas Ganguli from RRCAT is thanked for all the support and encouragement.

-
- [1] F. Wilczek, Two applications of axion electrodynamics, *Phys. Rev. Lett.* **58**, 1799 (1987).
- [2] R. S. K. Mong, A. M. Essin, and J. E. Moore, Antiferromagnetic topological insulators, *Phys. Rev. B* **81**, 245209 (2010).
- [3] R. Li, J. Wang, X.-L. Qi, and S.-C. Zhang, Dynamical axion field in topological magnetic insulators, *Nature Physics* **6**, 284 (2010).
- [4] R. Yu, W. Zhang, H.-J. Zhang, S.-C. Zhang, X. Dai, and Z. Fang, Quantized Anomalous Hall Effect in Magnetic Topological Insulators, *Science* **329**, 61 (2010).
- [5] C.-Z. Chang, J. Zhang, X. Feng, J. Shen, Z. Zhang, M. Guo, K. Li, Y. Ou, P. Wei, L.-L. Wang, Z.-Q. Ji, Y. Feng, S. Ji, X. Chen, J. Jia, X. Dai, Z. Fang, S.-C. Zhang, K. He, Y. Wang, L. Lu, X.-C. Ma, and Q.-K. Xue, Experimental Observation of the Quantum Anomalous Hall Effect in a Magnetic Topological Insulator, *Science* **340**, 167 (2013).
- [6] Z. F. Wang, Z. Liu, and F. Liu, Quantum Anomalous Hall Effect in 2D Organic Topological Insulators, *Phys. Rev. Lett.* **110**, 196801 (2013).
- [7] X.-L. Qi and S.-C. Zhang, Topological insulators and superconductors, *Rev. Mod. Phys.* **83**, 1057 (2011).
- [8] X. Wan, A. M. Turner, A. Vishwanath, and S. Y. Savrasov, Topological semimetal and Fermi-arc surface states in the electronic structure of pyrochlore iridates, *Phys. Rev. B* **83**, 205101 (2011).
- [9] H. Zhang, J. Wang, G. Xu, Y. Xu, and S.-C. Zhang, Topological States in Ferromagnetic CdO/EuO Superlattices and Quantum Wells, *Phys. Rev. Lett.* **112**, 096804 (2014).
- [10] K. Kuroda, T. Tomita, M.-T. Suzuki, C. Bareille, A. Nugroho, P. Goswami, M. Ochi, M. Ikhlas, M. Nakayama, S. Akebi, *et al.*, Evidence for magnetic Weyl fermions in a correlated metal, *Nature materials* **16**, 1090 (2017).
- [11] C.-Z. Chang, W. Zhao, D. Y. Kim, H. Zhang, B. A. Assaf, D. Heiman, S.-C. Zhang, C. Liu, M. H. Chan, and J. S. Moodera, High-precision realization of robust quantum anomalous Hall state in a hard ferromagnetic topological insulator, *Nature materials* **14**, 473 (2015).
- [12] Terahertz spectroscopy on Faraday and Kerr rotations in a quantum anomalous Hall state, author=Okada, Ken N and Takahashi, Youtarou and Mogi, Masataka and Yoshimi, Ryutarou and Tsukazaki, Atsushi and Takahashi, Kei S and Ogawa, Naoki and Kawasaki, Masashi and Tokura, Yoshinori, *Nature communications* **7**, 1 (2016).
- [13] Magnetic topological insulators, author=Tokura, Yoshinori and Yasuda, Kenji and Tsukazaki, Atsushi, *Nature Reviews Physics* **1**, 126 (2019).
- [14] M. M. Otrokov, I. I. Klimovskikh, H. Bentmann, D. Estyunin, A. Zeugner, Z. S. Aliev, S. Gaß, A. Wolter, A. Koroleva, A. M. Shikin, *et al.*, Prediction and observation of an antiferromagnetic topological insulator, *Nature* **576**, 416 (2019).
- [15] Y. Gong, J. Guo, J. Li, K. Zhu, M. Liao, X. Liu, Q. Zhang, L. Gu, L. Tang, X. Feng, D. Zhang, W. Li, C. Song, L. Wang, P. Yu, X. Chen, Y. Wang, H. Yao, W. Duan, Y. Xu, S.-C. Zhang, X. Ma, Q.-K. Xue, and K. He, Experimental Realization of an Intrinsic Magnetic Topological Insulator, *Chinese Physics Letters* **36**, 076801 (2019).
- [16] A. Zeugner, F. Nietschke, A. U. Wolter, S. Gaß, R. C. Vidal, T. R. Peixoto, D. Pohl, C. Damm, A. Lubk, R. Hentrich, *et al.*, Chemical aspects of the candidate antiferromagnetic topological insulator MnBi_2Te_4 , *Chemistry of Materials* **31**, 2795 (2019).
- [17] Y. Deng, Y. Yu, M. Z. Shi, Z. Guo, Z. Xu, J. Wang, X. H. Chen, and Y. Zhang, Quantum anomalous Hall effect in intrinsic magnetic topological insulator MnBi_2Te_4 , *Science* **367**, 895 (2020).
- [18] S. H. Lee, Y. Zhu, Y. Wang, L. Miao, T. Pillsbury, H. Yi, S. Kempinger, J. Hu, C. A. Heikes, P. Quarterman, W. Ratcliff, J. A. Borchers, H. Zhang, X. Ke, D. Graf, N. Alem, C.-Z. Chang, N. Samarth, and Z. Mao, Spin scattering and noncollinear spin structure-induced intrinsic anomalous Hall effect in antiferromagnetic topological insulator MnBi_2Te_4 , *Phys. Rev. Research* **1**, 012011 (2019).
- [19] D. Zhang, M. Shi, T. Zhu, D. Xing, H. Zhang, and J. Wang, Topological Axion States in the Magnetic Insulator MnBi_2Te_4 with the Quantized Magnetoelectric Effect, *Phys. Rev. Lett.* **122**, 206401 (2019).
- [20] J.-Q. Yan, Q. Zhang, T. Heitmann, Z. Huang, K. Y. Chen, J.-G. Cheng, W. Wu, D. Vaknin, B. C. Sales, and R. J. McQueeney, Crystal growth and magnetic structure of MnBi_2Te_4 , *Phys. Rev. Materials* **3**, 064202 (2019).
- [21] Y.-J. Hao, P. Liu, Y. Feng, X.-M. Ma, E. F. Schwier, M. Arita, S. Kumar, C. Hu, R. Lu, M. Zeng, Y. Wang, Z. Hao, H.-Y. Sun, K. Zhang, J. Mei, N. Ni, L. Wu, K. Shimada, C. Chen, Q. Liu, and C. Liu, Gapless Surface Dirac Cone in Antiferromagnetic Topological Insulator MnBi_2Te_4 , *Phys. Rev. X* **9**, 041038 (2019).
- [22] Y. J. Chen, L. X. Xu, J. H. Li, Y. W. Li, H. Y. Wang, C. F. Zhang, H. Li, Y. Wu, A. J. Liang, C. Chen, S. W. Jung, C. Chao, Y. H. Mao, S. Liu, M. X. Wang, Y. F. Guo, Y. Xu, Z. K. Liu, L. X.

- Yang, and Y. L. Chen, Topological Electronic Structure and Its Temperature Evolution in Antiferromagnetic Topological Insulator MnBi_2Te_4 , *Phys. Rev. X* **9**, 041040 (2019).
- [23] Jiazhen Wu and Fucai Liu and Masato Sasase and Koichiro Ienaga and Yukiko Obata and Ryu Yukawa and Koji Horiba and Hiroshi Kumigashira and Satoshi Okuma and Takeshi Inoshita and Hideo Hosono, Natural van der waals heterostructural single crystals with both magnetic and topological properties, *Science Advances* **5**, eaax9989 (2019).
- [24] J. Li, C. Wang, Z. Zhang, B.-L. Gu, W. Duan, and Y. Xu, Magnetically controllable topological quantum phase transitions in the antiferromagnetic topological insulator MnBi_2Te_4 , *Phys. Rev. B* **100**, 121103 (2019).
- [25] J.-Q. Yan, Z. Huang, W. Wu, and A. May, Vapor transport growth of MnBi_2Te_4 and related compounds, *Journal of Alloys and Compounds* **906**, 164327 (2022).
- [26] C. Liu, Y. Wang, H. Li, Y. Wu, Y. Li, J. Li, K. He, Y. Xu, J. Zhang, and Y. Wang, Robust axion insulator and Chern insulator phases in a two-dimensional antiferromagnetic topological insulator, *Nature materials* **19**, 522 (2020).
- [27] H. Li, S. Liu, C. Liu, J. Zhang, Y. Xu, R. Yu, Y. Wu, Y. Zhang, and S. Fan, Antiferromagnetic topological insulator MnBi_2Te_4 : synthesis and magnetic properties, *Phys. Chem. Chem. Phys.* **22**, 556 (2020).
- [28] OrujluE., Phase equilibria in the SnBi_2Te_4 - MnBi_2Te_4 system and characterization of the $\text{Sn}_{1-x}\text{Mn}_x\text{Bi}_2\text{Te}_4$ solid solutions, *Physics and Chemistry of Solid State* **21**, 113 (2020).
- [29] M. Ahmad, K. Agarwal, and B. R. Mehta, An anomalously high Seebeck coefficient and power factor in ultrathin Bi_2Te_3 film: Spin-orbit interaction, *Journal of Applied Physics* **128**, 035108 (2020), <https://doi.org/10.1063/5.0007440>.
- [30] P.-Y. Chuang, S.-H. Su, C.-W. Chong, Y.-F. Chen, Y.-H. Chou, J.-C.-A. Huang, W.-C. Chen, C.-M. Cheng, K.-D. Tsuei, C.-H. Wang, Y.-W. Yang, Y.-F. Liao, S.-C. Weng, J.-F. Lee, Y.-K. Lan, S.-L. Chang, C.-H. Lee, C.-K. Yang, H.-L. Su, and Y.-C. Wu, Anti-site defect effect on the electronic structure of a Bi_2Te_3 topological insulator, *RSC Adv.* **8**, 423 (2018).
- [31] V. Neudachina, T. Shatalova, V. Shtanov, L. Yashina, T. Zyubina, M. Tamm, and S. Kobeleva, Xps study of $\text{SnTe}(100)$ oxidation by molecular oxygen, *Surface Science* **584**, 77 (2005), selected papers of the Fifth Nordic Conference on Surface Science (NCSS-5).
- [32] R. Iwanowski, M. Heinonen, and E. Janik, X-ray photoelectron spectra of zinc-blende mnte , *Chemical Physics Letters* **387**, 110 (2004).
- [33] F. Jiao, J. Wang, X. Wang, Q. Tian, M. Chang, L. Cai, S. Zhu, D. Zhang, Q. Lu, C. Wang, *et al.*, The layer-inserting growth of antiferromagnetic topological insulator MnBi_2Te_4 based on symmetry and its x-ray photoelectron spectroscopy, *Journal of Superconductivity and Novel Magnetism* **34**, 1485 (2021).
- [34] J. Zhu, M. Naveed, B. Chen, Y. Du, J. Guo, H. Xie, and F. Fei, Magnetic and electrical transport study of the antiferromagnetic topological insulator Sn-doped MnBi_2Te_4 , *Phys. Rev. B* **103**, 144407 (2021).
- [35] J. M. D. Coey, *Magnetism and Magnetic Materials* (Cambridge University Press, 2010).
- [36] A. Tan, V. Labracherie, N. Kunchur, A. U. B. Wolter, J. Cornejo, J. Dufouleur, B. Büchner, A. Isaeva, and R. Giraud, Metamagnetism of Weakly Coupled Antiferromagnetic Topological Insulators, *Phys. Rev. Lett.* **124**, 197201 (2020).
- [37] J.-Q. Yan, S. Okamoto, M. A. McGuire, A. F. May, R. J. McQueeney, and B. C. Sales, Evolution of structural, magnetic, and transport properties in $\text{MnBi}_{2-x}\text{Sb}_x\text{Te}_4$, *Phys. Rev. B* **100**, 104409 (2019).
- [38] S. Chakraborty and A. K. Majumdar, Resistivity minima in concentrated $\gamma\text{-Cu}_{100-x}\text{Mn}_x$ alloys ($36 \leq x \leq 83$), *Phys. Rev. B* **53**, 6235 (1996).
- [39] E. Abrahams, P. W. Anderson, D. C. Licciardello, and T. V. Ramakrishnan, Scaling Theory of Localization: Absence of Quantum Diffusion in Two Dimensions, *Phys. Rev. Lett.* **42**, 673 (1979).
- [40] J. Kondo, Resistance minimum in dilute magnetic alloys, *Prog. Theor. Phys.* **32**, 37 (1964).
- [41] K. Ciesielski, D. Gnida, H. Borrmann, R. Ramlau, Y. Prots, D. Szymański, Y. Grin, and D. Kaczorowski, Structural, thermodynamic and magnetotransport properties of half-Heusler compound HoPtSb , *J Alloy Compd* **829**, 154467 (2020).
- [42] H. Liu, L. Bao, Z. Zhou, B. Che, R. Zhang, C. Bian, R. Ma, L. Wu, H. Yang, J. Li, C. Gu, C.-M. Shen, S. Du, and H.-J. Gao, Quasi-2D Transport and Weak Antilocalization Effect in Few-layered VSe_2 , *Nano Letters* **19**, 4551 (2019), pMID: 31241975.
- [43] R. R. Jia, J. C. Zhang, R. K. Zheng, D. M. Deng, H.-U. Habermeier, H. L. W. Chan, H. S. Luo, and S. X. Cao, Effects of ferroelectric-poling-induced strain on the quantum correction to low-temperature resistivity of manganite thin films, *Phys. Rev. B* **82**, 104418 (2010).
- [44] B. Kuropatwa and H. Kleinke, Thermoelectric Properties of Stoichiometric Compounds in the $(\text{SnTe})_x(\text{Bi}_2\text{Te}_3)_y$ System, *Zeitschrift für anorganische und allgemeine Chemie* **638**, 2640 (2012).
- [45] Y.-C. Zou, Z.-G. Chen, E. Zhang, F. Kong, Y. Lu, L. Wang, J. Drennan, Z. Wang, F. Xiu, K. Cho, *et al.*, Atomic disorders in layer structured topological insulator SnBi_2Te_4 nanoplates, *Nano Research* **11**, 696 (2018).
- [46] J.-Y. Tak, Y. S. Lim, J. N. Kim, C. Lee, J. H. Shim, H. K. Cho, C.-H. Park, and W.-S. Seo, Thermoelectric transport properties of tetradymite-type $\text{Pb}_{1-x}\text{Sn}_x\text{Bi}_2\text{Te}_4$ compounds, *Journal of Alloys and Compounds* **690**, 966 (2017).
- [47] Y.-J. Hao, P. Liu, Y. Feng, X.-M. Ma, E. F. Schwier, M. Arita, S. Kumar, C. Hu, R. Lu, M. Zeng, Y. Wang, Z. Hao, H.-Y. Sun, K. Zhang, J. Mei, N. Ni, L. Wu, K. Shimada, C. Chen, Q. Liu, and C. Liu, Gapless Surface Dirac Cone in Antiferromagnetic Topological Insulator MnBi_2Te_4 , *Phys. Rev. X* **9**, 10.1103/physrevx.9.041038 (2019).
- [48] A. M. Shikin, D. Estyunin, I. I. Klimovskikh, S. Filnov, E. Schwier, S. Kumar, K. Miyamoto, T. Okuda, A. Kimura, K. Kuroda, *et al.*, Nature of the Dirac gap modulation and surface magnetic interaction in axion antiferromagnetic topological insulator MnBi_2Te_4 , *Scientific Reports* **10**, 1 (2020).
- [49] C. Trang, Q. Li, Y. Yin, J. Hwang, G. Akhgar, I. Di Bernardo, A. Grubisic Cabo, A. Tadich, M. Fuhrer, S.-K. Mo, N. Medhekar, and M. Edmonds, Crossover from 2D ferromagnetic insulator to wide bandgap quantum anomalous Hall insulator in ultra-thin MnBi_2Te_4 , *ACS Nano* **15** (2021).
- [50] B. Chen, F. Fei, D. Zhang, B. Zhang, W. Liu, S. Zhang, P. Wang, B. Wei, Y. Zhang, Z. Zuo, *et al.*, Intrinsic magnetic topological insulator phases in the Sb doped MnBi_2Te_4 bulks and thin flakes, *Nature communications* **10**, 1 (2019).
- [51] K. G. S. Ranmohotti, H. Djieutedjeu, and P. F. P. Poudeu, ChemInform abstract: Chemical manipulation of magnetic ordering in $\text{mn}_{1-x}\text{Sn}_x\text{Bi}_2\text{se}_4$ solid-solution., *ChemInform* **44**, no (2013).